Signal and measurement considerations for human translation of diffuse *in vivo* flow cytometry

Fernando Ivich, Joshua Pace, Amber L. Williams, Malcolm Shumel, Qianqian Fang, and Mark Niedre*

Northeastern University, Department of Bioengineering, Boston, Massachusetts, United States

Abstract

Significance: "Diffuse *in vivo* flow cytometry" (DiFC) is an emerging technology for fluorescence detection of rare circulating cells directly in large deep-seated blood vessels in mice. Because DiFC uses highly scattered light, in principle, it could be translated to human use. However, an open question is whether fluorescent signals from single cells would be detectable in human-scale anatomies.

Aim: Suitable blood vessels in a human wrist or forearm are at a depth of ~2 to 4 mm. The aim of this work was to study the impact of DiFC instrument geometry and wavelength on the detected DiFC signal and on the maximum depth of detection of a moving cell.

Approach: We used Monte Carlo simulations to compute fluorescence Jacobian (sensitivity) matrices for a range of source and detector separations (SDS) and tissue optical properties over the visible and near infrared spectrum. We performed experimental measurements with three available versions of DiFC (488, 640, and 780 nm), fluorescent microspheres, and tissue mimicking optical flow phantoms. We used both computational and experimental data to estimate the maximum depth of detection at each combination of settings.

Results: For the DiFC detection problem, our analysis showed that for deep-seated blood vessels, the maximum sensitivity was obtained with NIR light (780 nm) and 3-mm SDS.

Conclusions: These results suggest that—in combination with a suitable molecularly targeted fluorescent probes—circulating cells and nanosensors could, in principle, be detectable in circulation in humans.

 [DOI: 10.1117/1.JBO.27.6.067001]

Keywords: Monte Carlo simulations; diffuse fluorescence; diffuse *in vivo* flow cytometry; optical devices.

Paper 220066R received Mar. 24, 2022; accepted for publication May 27, 2022; published online Jun. 20, 2022.

1 Introduction

Diffuse *in vivo* flow cytometry (DiFC)[1,2] is an emerging technique that uses diffusely scattered light to continuously and non-invasively detect and count fluorescence-labeled (and fluorescent protein expressing) cells in the blood of small animals. The DiFC uses optical fiber bundles ("probes") to generate and measure laser induced fluorescent light from individual cells moving in blood vessels, for example in the mouse tail artery [Fig. 1(a)].[3] A unique property of DiFC is that it allows sampling of the full peripheral blood volume of a mouse in about 15 min. A major application is therefore the non-invasive enumeration of rare circulating tumor cells (CTCs), which have been found to be instrumental in hematogenous metastasis but typically number fewer than 100 cells per ml of peripheral blood. We previously used DiFC to detect rare CTCs in xenograft models[4,5] and observe changes in CTC numbers over time.[6] We also used

*Address all correspondence to Mark Niedre, m.niedre@neu.edu

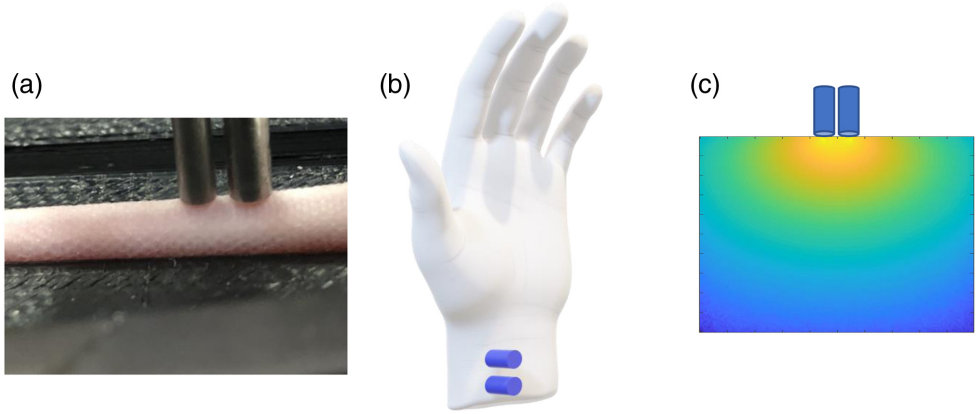

Fig. 1 (a) Photograph of DiFC probes on the ventral surface of a mouse tail. We use DiFC to detect rare fluorescently labeled CTCs in the ventral caudal artery. (b) Conceptual schematic showing DiFC use in human wrists where blood vessels are 2 to 4 mm in depth. (c) Qualitative example of sensitivity profile (Jacobian matrix) for a 3-mm SDS.

DiFC with engineered optical sensors that circulate in the blood to measure systemic sodium levels.[7]

Because DiFC uses diffuse light and works in an epi-illumination (as opposed to trans-illumination) geometry, in principle, it could be used in larger species, including humans.[8] If feasible, DiFC could provide a new method to continuously enumerate rare CTCs[9–11] directly *in vivo* without having to draw and analyze blood samples.[12] Fluorescent labeling of CTCs for DiFC could be achieved using cancer-specific fluorescence contrast agents such as those in development for fluorescence-guided surgery.[13,14] Our lab showed that it is feasible to label CTCs directly in mice with a small-molecule folate-targeted fluorescent probe (EC-17), and detect them externally with our DiFC system.[15]

However, translation of DiFC to humans would also entail detecting light from deeper-seated blood vessels compared to those in mice. Specifically, we have used DiFC on arteries in the tail or leg in mice, which are ~0.75 to 1 mm in depth. Suitable candidate blood vessels in a human include the radial artery or vein in the human wrist, which are about 2 to 4 mm in depth[16] [Fig. 1(b)]. These are easily observed visually from the skin surface, facilitating simple potential alignment of DiFC probes. Typical flow rates in these vessels are in the range of 100 ml per minute.[17] As such, in principle, this would permit sampling of 1 liter of circulating blood (equivalent to about 20% of the peripheral blood volume) in a 10 min scan. An open question is therefore whether single cells would be detectable with DiFC, since the fluorescent signal is expected to be significantly attenuated due to light scatter and absorption [Fig. 1(c)]. In addition, the ratio of the signal from a single cell to the background (non-specific) tissue autofluorescence is expected to be lower at deeper blood vessel depths.

As described in more detail below, our small animal DiFC design uses an integrated multi-fiber probe, where the source and detector fiber positions are physically adjacent (0.3-mm center-to-center separation). Previous work in the near-infrared spectroscopy (functional NIRS) fields have extensively studied the effect of different fiber probe geometries on the optical sensitivity of human tissue.[18] In particular, NIRS and diffuse optical tomography (DOT) frequently use larger source and detector separations (SDS) to probe deeper tissue volumes,[19–21] e.g., in the brain.[22,23] Biological tissue is a high albedo medium, meaning that scattering strongly dominates absorption. As such, the path of a visible or near-infrared photon can be thought of as a random walk with forward biased scattering. In general, photons detected on the tissue surface will preferentially have traveled deeper in tissue for longer separations from the source positions. However, it is unclear to what degree this approach is applicable for the specific DiFC detection problem. It is also broadly understood that red and near infrared (NIR) light undergoes less attenuation in tissue than visible light.[24,25] This effect can be computed explicitly as we do here.

The purpose of this work was to use Monte Carlo (MC) photon transport simulations and experimental optical phantom models to (i) study the effect of laser (and fluorophore)

wavelengths, and light SDS on the detection problem in DiFC, and (ii) assess whether, in principle, CTCs could be detectable in appropriate blood vessels in humans.

2 Materials and Methods

2.1 *Diffuse* In Vivo *Flow Cytometer*

DiFC instrumentation has been described in detail by our team previously.[1,4,6,7] Thus far, we have developed blue-green[4] (488-nm laser), red[1] (640-nm laser), and NIR[26] (780-nm laser) versions, designed to work with different widely used fluorophores and fluorescent proteins. Briefly, DiFC uses laser light which is coupled into an optical fiber to illuminate a sample surface (i.e., skin). As fluorescently labeled cells pass through the field-of-view, they emit fluorescent light which is detected with a separate set of eight detection fibers. Each fiber tip has miniaturized integrated filters to minimize leakage of laser light into the collection fiber. The output is filtered and detected with photomultiplier tubes (PMTs).

The present DiFC design uses an integrated fiber probe (bundle)[1,4] where the source and detector fibers are assembled in circular arrangement with center-to-center separation of 0.3 mm [Fig. 2(a)]. For SDS of 3 mm or larger, we used two separate fiber probes—one as the excitation source (with detector fibers deactivated) and the second for collection and detection of fluorescent light only (with the source fiber deactivated).

2.2 *Monte Carlo Light Transport Simulations*

The MC simulations of photon propagation in three-dimensional (3D) tissue volumes were performed using Monte Carlo eXtreme (MCX) software.[27,28] MCX is an open-source MC simulator that accelerates computational efficiency via parallel processing using a graphic processing unit. Simulations involved using a cubic homogeneous $5 \times 5 \times 5$ cm^3 volume representing a portion of a human arm, with an isotropic voxel size dV of $250 \times 250 \times 250$ μm^3. The optical properties for a selective set of wavelengths within the visible and NIR spectrum were chosen from the literature.[29] The refractive index and anisotropy coefficient were chosen to be 1.37 and 0.9, respectively, for all tested wavelengths. Table 1 shows the optical properties used for the studies here. Although there is of course a wavelength red-shift between excitation and emission laser light, this effect is negligible compared to the uncertainties in the values (see discussion below).[29,30] For each simulation, a total of 10^8 photon packets were simulated with a time gate of 5 ns.

Each element of the fluorescence sensitivity matrix (Jacobian) $W^{fl}(r_j; r_s, r_d)$ reflects the magnitude of the detection signal change for a given source (located at r_s) detector (located at r_d) pair for a unitary fluorescence yield perturbation $\eta_{fl}(r_j)$ at a given location r_j in the volume Ω_j. This was computed via the adjoint Monte Carlo method. A Born approximation-based Jacobian based on the adjoint method was described in detail previously.[31] Here, we applied the Born approximation, and the continuous wave Jacobian can be given as

$$W^{fl}(r; r_s, r_d) = \int_{\Omega_j} G^{ex}(r_j, r_s) G^{em}(r_d, r_j) \mathrm{d}V, \tag{1}$$

where $G^{ex}(r_j, r_s)$ is the Green's function at the excitation wavelength defined at any position r_j in the medium illuminated by a unitary source at position r_s, $G^{em}(r_d, r_j)$ is the Green's function at the emission wavelength measured at the detector position r_d as a result of the emitted light from the medium originated at point r_j. For all medium locations r_j, $G^{em}(r_d; r_j)$ values were conveniently computed by a single forward solution $G^{em}(r_j; r_d)$ by setting the source at the detector location r_d, as a result of reciprocity, i.e., $G^{em}(r_d; r_j) = G^{em}(r_j; r_d)$. Both Green's functions were computed using MCX with the wavelength dependent optical properties above. We repeated the above calculations for a range of SDS ranging from 0.3 to 12 mm on the surface of the volume. The extracted voxel-based sensitivity values from the simulations were taken from

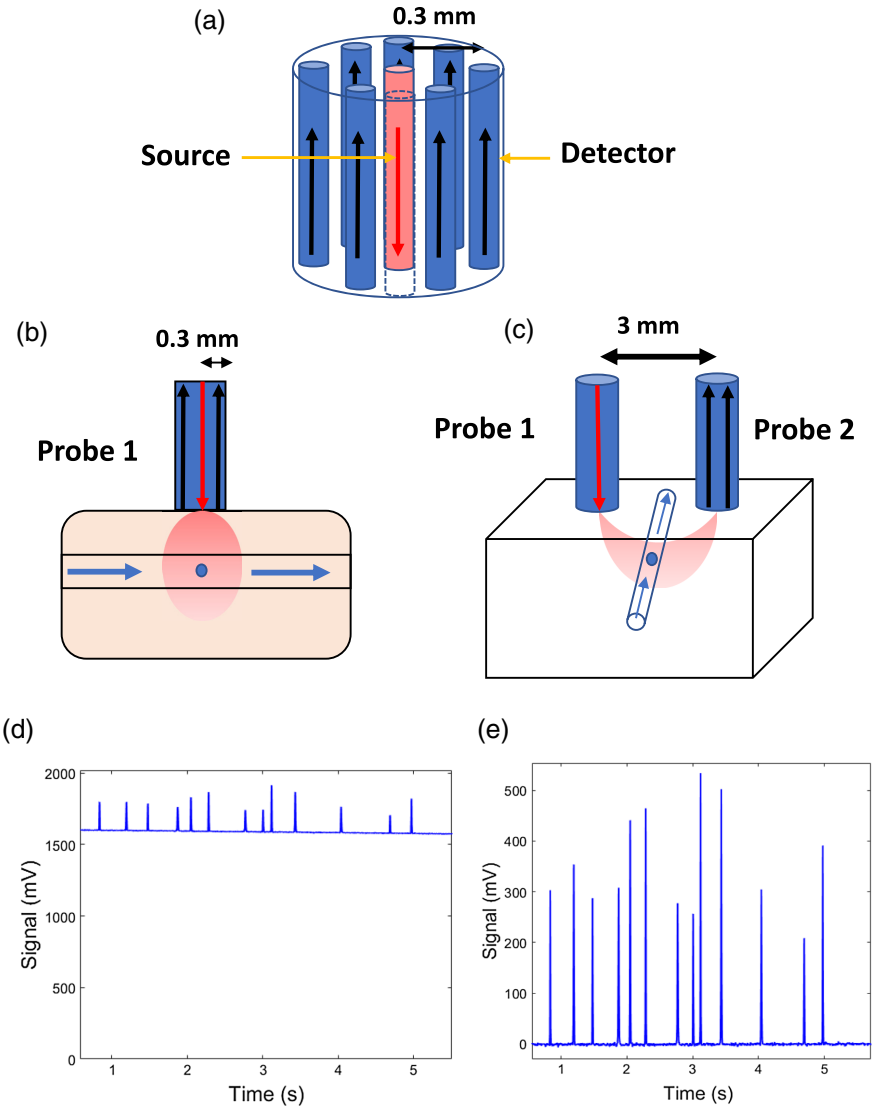

Fig. 2 DiFC. (a) Diagram of DiFC fiber probe showing the detector fibers in black and the source fiber in red. (b) 0.3-mm SDS configuration for DiFC. The DiFC fiber probe is showing the laser source (red arrow) and detector (black arrows) separated by 0.3 mm. (c) Two DiFC fiber probes separated by 3 mm. Fiber probe 1 has a light source (red arrow) and fiber probe 2 has photodetectors (black arrows) separated by 3 mm. (d) Non-background-subtracted sample data showing cell detections as peaks. (e) Background-subtracted sample data showing the same cell detections.

Table 1 Absorption (μ_a) and scattering (μ_s) coefficients used for the DiFC Monte Carlo simulations. The anisotropy coefficient, g, and the index of refraction, n, were 0.9 and 1.37, respectively, in all cases.[28]

	Blue-green 488 nm	Red 640 nm	NIR 780 nm
μ_a (mm^{-1})	0.05	0.025	0.002
μ_s (mm^{-1})	25	10	7

the middle point between source and detector along the depth of the simulated tissue, as shown in Figs. 2(b) and 2(c).

2.3 *Contrast (Signal to Background Ratio) Estimation*

To explore theoretical limits of detection, we estimated the sensitivity ratio between a fluorescent peak and the background autofluorescence as follows. Following the first-order Born approximation, this linearized formulation follows the equation $\Phi_{fl}(r_d, r_s) = W^{fl}(r_j; r_s, r_d)\,\eta_{fl}(r_j)$, where $\Phi_{fl}(r_d, r_s)$ is the measured fluorescence signal between a given source and detector pair.

We further assume that this fluorescence signal is the sum of the contribution of the transient fluorescence peak from a moving cell and the non-specific background autofluorescence:

$$\Phi_{fl} = \Phi_{fl-pk} + \Phi_{fl-af} \tag{2}$$

To estimate the signal for a cell detection (peak) $\Phi_{fl-pk}(r_d, r_s)$ at depth in the media d, we assumed $\eta(r_j) = \eta_{\text{cell}}$ for $r_j = (0, 0, \text{d})$, and $\eta(r_j) = 0$ elsewhere. It is noteworthy that the diameter of a cell is much smaller than the voxel size used here. To estimate η_{cell} we used experimental DiFC measurements as detailed below.

To estimate the background autofluorescence signal $\Phi_{fl-af}(r_d, r_s)$, we made the simplifying assumption that autofluorescence was constant throughout the media η_{af}. This was also estimated using experimental measurements. It is noteworthy that both η_{cell} and η_{af} were assumed to be different for the 488-, 640-, and 780-nm systems.

2.4 *Optical Phantom Models* In Vitro

To experimentally test the relationships between target depth, SDS distance, and wavelength, we used a tissue mimicking optical phantom made of high-density polyethylene. We have previously shown that this material has optical properties similar to biological tissues.[1] The phantom has drilled holes at different depths ranging from 0.75- to 4-mm deep where we thread microbore Tygon tubing (TGY-010-C, Small Parts, Inc., Seattle, Washington) to simulate a blood vessel. The tubing is connected to a syringe pump (70-2209, Harvard Apparatus, Holliston, Massachusetts) where we flow fluorescent microspheres to mimic fluorescently labeled cells,[1,4] or optical sensors. We suspended the fluorescent microsphere solution in phosphate buffer saline (PBS) at a concentration of 10^3 microspheres per milliliter and flowed them at a rate of 50-μl per minute. We used Flash Red reference intensity 5 (FR5; Bangs Laboratories Inc., Fisher, Indiana), Dragon Green reference intensity 5 (DG5; Bangs), and Jade Green high intensity (Spherotech Inc., Lake Forest, Illinois) microspheres for red, blue-green, and NIR wavelengths, respectively. We showed previously that these approximate the fluorophore brightness of a well-labeled cell.[1,15] We also used performed control experiments with PBS only (no microspheres) to determine the instrument false alarm rate. We performed $N = 5$ replicates for each wavelength combination, SDS, and microsphere-depth.

In Fig. 2, we include a schematic of the DiFC fiber probe showing the source fiber and the detector fibers [Fig. 2(a)]. Example configurations for 0.3- and 3-mm SDS are shown in Figs. 2(b) and 2(c), respectively. The tubing is placed in the middle of the two probes, running in a perpendicular direction. Figure 2(d) shows example measured data, and Fig. 2(e) shows the data after mean background subtraction. When increasing the SDS separation, we also increased the PMT sensitivity gain to approximately match the background autofluorescence. The laser power at the sample surface was 20 mW for all experiments.

2.5 *DiFC Data Analysis*

DiFC data were analyzed as described previously.[4] Briefly, the signal processing algorithm follows the following steps:

1. Subtraction of the signal background; this is done by subtraction of the signal moving median value with 5 s window [as in Figs. 2(d) and 2(e)]

2. Calculation of the signal noise post background subtraction with a 1 min moving window
3. Identification of peak candidates with a threshold above five times the local noise, which gives a minimum signal to noise ratio (SNR) of $20\log_{10}(5) = 13.9$ dB.

In addition, when used *in vivo*, we use two DiFC probes and apply an additional matching condition for detections. Peak candidates from the probes are matched in either the forward or reverse direction based on the peak amplitude, width, and transit time between the detectors. Peaks that are not matched are discarded from the analysis. This ensures that detected peaks are from cells moving in target arteries or veins. Unmatched peaks are normally from detected cells in the capillary bed or other small blood vessels. This also discards spurious signals due to instrument noise or motion artifacts. Endogenous autofluorescence from biological tissue is generally constant over the timescale of seconds (as opposed to transient fluorescent peaks from CTCs). Hence these contribute to the background signal and are subtracted off in step 1 above.

3 Results

3.1 *Monte Carlo Simulations*

Sensitivity matrices were computed for 488-, 640-, and 780-nm excitation wavelengths and for different SDS values as summarized in Fig. 3. Figures 3(a), 3(c), and 3(e) show example sensitivity matrices for SDS of 0.3, 3, and 6 mm, respectively. Figures 3(b), 3(d), and 3(f) show the sensitivity as a function of depth (up to 5 mm) at the center line between the fibers at 488, 640, and 780 nm for the same SDS. These data are normalized to the maximum sensitivity value along the midline between source and detector, for all combinations, in this case 0.3-mm SDS and 488-nm wavelength. The effects of SDS on the depth sensitivity of tissue are summarized in Figs. 3(g) and 3(h). As expected, these results showed that the depth of maximum sensitivity increased with increased SDS [Fig. 3(g)]. While these data nominally suggest that deeper cell sensitivity could be achieved using larger SDS, we note that the absolute value of the sensitivity also decreased strongly (by ~3 orders of magnitude) for larger SDS [Fig. 3(h)]. Likewise, the absolute value of sensitivity generally decreased with shorter wavelengths due to higher light attenuation [Fig. 3(h)]. The implications of these for the DiFC detection problem are discussed in more detail in Sec. 3.3 below.

3.2 *DiFC Measurements in Phantoms* In Vitro

We next used our three DiFC systems to experimentally test the same relationships in a tissue-mimicking flow phantom model.[1,4] Figure 4 shows the normalized MC sensitivity calculations and experimental measurement of mean fluorescent microsphere peak amplitudes for 0.3- and 3-mm SDS. Specifically, Fig. 4(a) shows the mean peak amplitude of DG5 microspheres (symbols) measured with DiFC with MC sensitivity calculations (solid line) for 488- and 0.3-mm SDS. Figure 4(b), shows the same with 3-mm SDS. Likewise, Figs. 4(c) and 4(d) show the same relationships for FR5 microspheres and 640-nm MC calculations, and Figs. 4(e) and 4(f) show the same relationships for Jade Green microspheres and 780-nm MC calculations. Here, each solid data point shows the average, and standard deviation from $N = 5$ measurements. It is noteworthy that no data points are shown for experiments without peak detections (which accounts for the different number of experimental points on each panel). For all wavelengths, the 0.3-mm SDS yielded greater signal amplitude at shallow target depths. We observed a small increase in amplitude for 780 nm for deeper targets for 3-mm SDS compared to 0.3 mm. The maximum detection depth was 2 mm for 488 and 640 nm, and 3.5 mm for 780 nm. For peaks of sufficiently low amplitude (near the instrument noise floor around 5 mV), it is likely that some microspheres were simply below the detection threshold of the system. To better illustrate this, we plotted the normalized (to maximum) detection count rate (per minute) for 0.3- and 3-mm SDS, in Figs. 5(a) and 5(b), respectively. As shown, the normalized count rate drops significantly at larger depths, and is more pronounced for lower wavelengths.

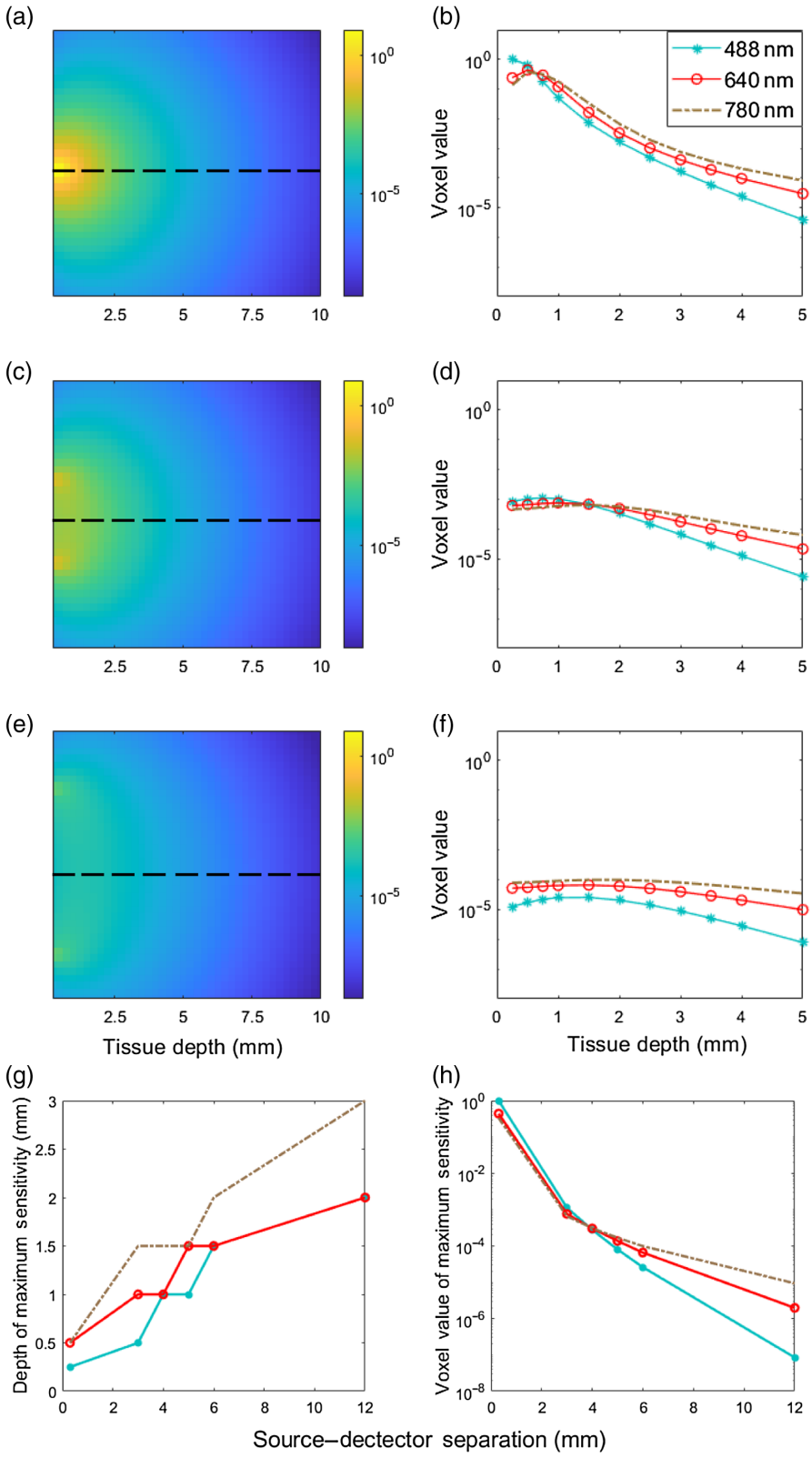

Fig. 3 MC simulations of photon propagation in a tissue-mimicking domain with SDS and optical properties as in Table 1. (a) Example sensitivity matrix for 0.3-mm SDS and 488-nm wavelength. (b) Sensitivity depth profile for SDS of 0.3 mm for 488, 640, and 780 nm. (c) and (d) Example sensitivity matrix and depth profiles for a 3-mm SDS. (e) and (f) Example sensitivity matrix and depth profile for a 6-mm SDS. (g) Depth of maximum sensitivity for different SDS. (h) Normalized (to the maximum along the midline) maximum sensitivity value for different SDS.

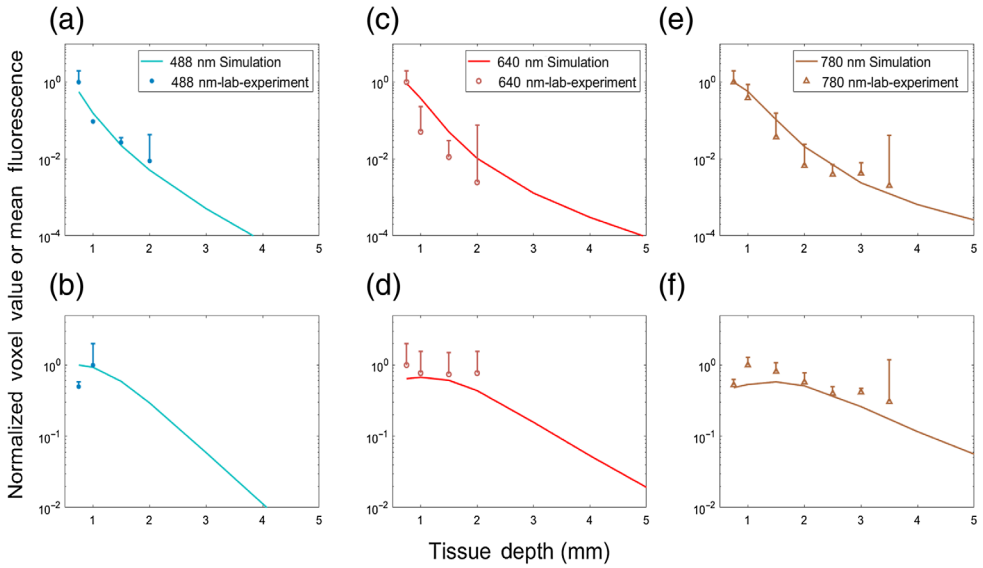

Fig. 4 (a), (c), and (e) Optical phantom measurements for 0.3 mm. (b), (d), and (f) 3-mm separations for 488-, 640-, and 780-nm wavelengths, respectively. The normalized MC simulated sensitivity and experimental measurements of mean DiFC peak intensity of microspheres for each are shown. The error bars represent the standard deviation.

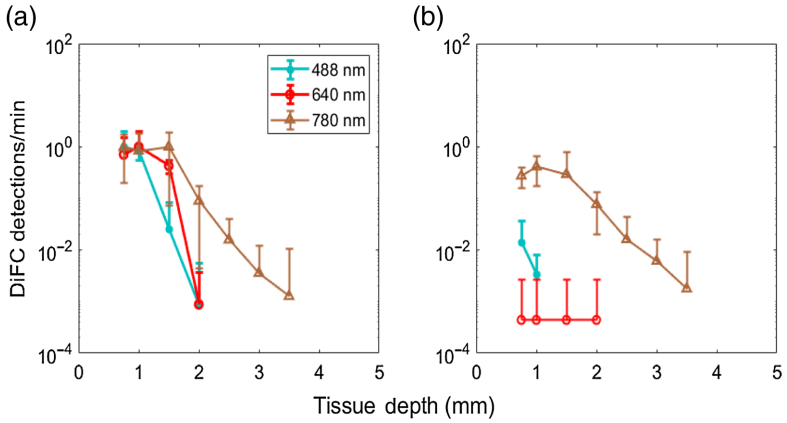

Fig. 5 Normalized microsphere detections per minute for nominally identical suspension concentrations for (a) 0.3- and (b) 3-mm SDS.

3.3 *Contrast to Background Analysis*

The DiFC detection problem relies on measurement of a small fluorescence signal from a single moving cell, on top of a larger non-specific background autofluorescence signal. This background is approximately constant over the timescale of a detected CTC peak (s). The magnitude of this autofluorescence varies with the laser wavelength and the type of tissue (e.g., mouse strain) in the experiment. While we subtract the mean of this background in data processing [as in Figs. 2(c) and 2(d)], the additive noise cannot be subtracted. The ratio of the expected peak amplitude from a single cell to this background noise therefore defines the lower level of detection sensitivity.

We can estimate this threshold for arbitrary SDS for each wavelength using our experimentally measured (phantom) data above and MC sensitivity functions. We estimated an average background autofluorescence concentration η_{af} in each case, which we assumed was homogeneous throughout the media to give the mean autofluorescence signal. We modeled additive

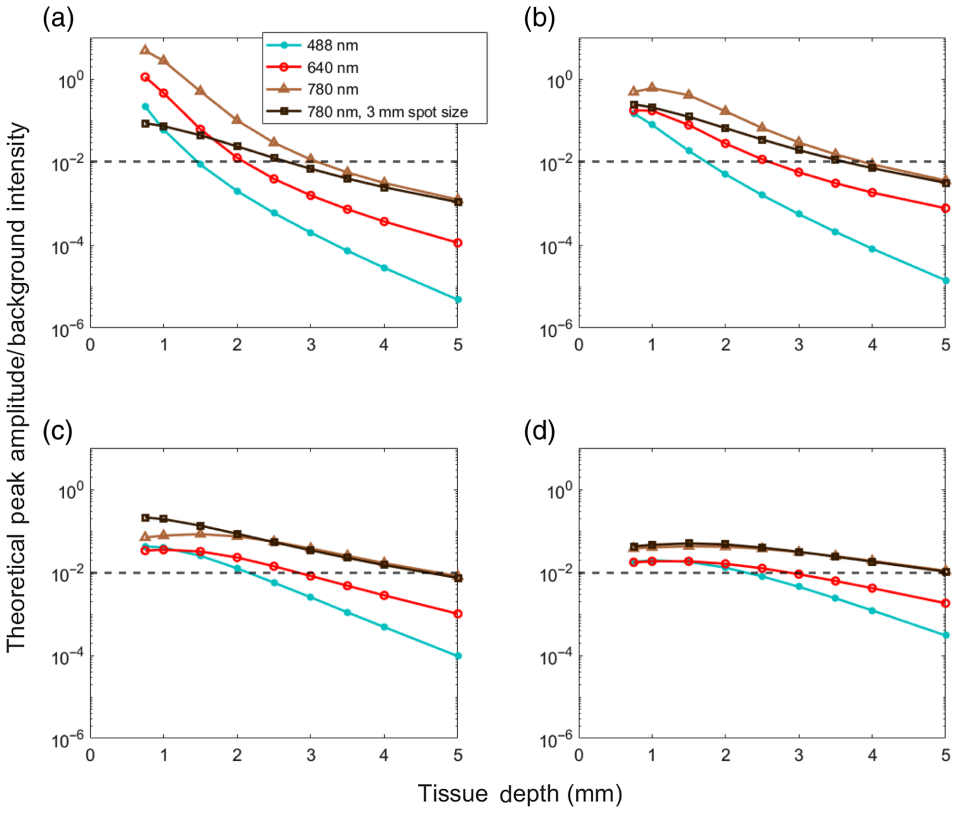

Fig. 6 Estimated signal to background ratios for red, blue-green, and NIR light. Horizontal lines represent the detection limit of 13.9 dB for (a) 0.3-, (b) 1-, (c) 3-, and (d) 5-mm SDS, respectively. The black curves show the sensitivity response if the excitation light was distributed over 3-mm diameter spot sizes in accordance with IEC exposure standards.

Gaussian noise, which based on our measurements with our existing DiFC prototypes, was a percentage of the average PMT signal output. Assuming a baseline (autofluorescence) signal output of 10% the maximum, the noise was equal to 0.2% of the background amplitude. We also estimated the average fluorescence concentration of a cell η_{cell} (which we assume was smaller than a voxel) to calculate the peak amplitude. We assumed that the minimum detectable peak was five times the noise (SNR = 13.9 dB). This threshold yielded a false alarm rate of 0.01 false positive detections per minute over all conditions tested. The results are summarized in Fig. 6.

As shown, the results are generally consistent with our experimental measurements. First, as expected, 780 nm yielded the highest peak to background ratio in all cases, followed by 640 and 488 nm. Second, use of larger SDS in general allowed detection of cells at larger depths particularly at longer wavelengths. Assuming cells were ~1 mm in depth (as is the case with our pre-clinical mouse experiments[4]), cells were expected to be detectable with all three wavelengths. If cells are expected to be 2 to 4 mm in depth (as expected in humans), then larger SDS are expected to yield higher peak-to-background ratios for 780 nm DiFC. Specifically, for 2-, 3-, and 4-mm deep cells, SDS of 1, 2, and 5 mm are expected to yield maximum sensitivity, and 2-mm SDS are expected to have best median sensitivity over the 2- to 4-mm depth range.

Another practical concern in potential application to humans is light power density and thermal safety. The International Electrotechnical Commission (IEC) laser safety standards permit exposure of approximately 300-mW per cm^2 in the NIR range. We currently use 20 mW of laser power; hence this would meet IEC standards if the power was distributed over 3-mm-diameter spot sizes (as opposed to 1 mm in our current DiFC design). As shown in Fig. 6 (black lines) the larger spot sizes would retain similar detection sensitivity in the 2- to 4-mm depth range for all SDS considered.

4 Discussion and Conclusions

We previously reported the use of DiFC exclusively in mice,[1,2,4,32] although an open question is whether DiFC could work in humans. The purpose of this work was to study whether tissue optics would permit detection of single cells in blood vessels 2- to 4-mm deep in diffuse tissue such as the radial[16] or ulnar artery or superficial facial arteries.[33] Moreover, the goal was to determine which SDS configuration and wavelengths of light would be most appropriate. Although the effect of fiber probe design has been widely studied for diffuse optical tomography applications,[19–21] we are unaware of any other theoretical and experimental study to explore the specific problem of diffuse fluorescence measurement from a single cell in bulk tissue.

Beyond DiFC, there are other technologies in development for optical detection of CTCs *in vivo*,[5] including photoacoustic methods[34,35] or intravital microscopy[36–38] with similar considerations for light attenuation in biological tissue. As noted, because DiFC works with diffuse light, it is expected to allow significantly greater depth-of-penetration compared to intravital confocal microscopy-based methods and is uniquely suited to human translation.

The MC studies here made the simplifying assumptions that the tissue was homogenous, and that the optical properties were the same for excitation and emission light. It also assumes that the background non-specific autofluorescence (particularly at superficial tissue depths) is approximately constant over the timescale of a CTC detection (s), which is valid in our prior experimental measurements. As shown, despite these assumptions our theoretical and experimental results were in good general agreement, and also consistent with our prior experimental work with DiFC in mice. This said, we tested how sensitive our conclusions were to the assumed optical properties by varying μ_a and μ_s by up to 50% for each combination. the estimated peak amplitude to background ratios (analogous to Fig. 6) for varying optical properties for 0.3- and 3-mm separation are shown in Figs. 7(a) and 7(b). As shown, varying the optical properties resulted in a change to the maximum estimated detection depth of 0.5 mm or less.

Likewise, we made the simplifying assumption that fluorescent microspheres used here approximated the brightness of a well-labeled (or fluorescent protein expressing) cell. This is generally consistent with our previous work.[1] In practice this brightness is a complex combination of fluorophore uptake by each cell,[39] extinction coefficient, quantum yield, and emission spectra match with the instrument optical filters, all of which would also naturally affect the maximum depth of detection in DiFC. To test this, we calculated the effect of detection depth if cells were either 50% brighter or 50% dimmer (η_{cell}) as summarized in Figs. 7(c) and 7(d). Increasing or decreasing the brightness may affect the maximum detection depth by as much as 1 mm. Likewise, our assumption of detectability relies on an assumption of instrument noise (0.2% of PMT output). In practice, noise may be higher in living organisms due to, for example, motion or photoplethysmography artifacts,[40] which in our experience is more pronounced in our Green Fluorescent Protein (GFP) compatible DiFC system. Likewise, the estimated detection limit could be improved with alternate signal processing approaches, reduction in instrument noise, or use of a lower threshold.

Overall, these studies showed two main practical insights for DiFC. First, for cases where cells are presumed to be at a shallow (<2 mm) depth, the use of a small (0.3 mm) SDS resulted in the highest sensitivity and allow use of green, red, and NIR wavelengths. Unsurprisingly, blue-green optical properties performed the worst, both due to the high non-specific tissue autofluorescence and the attenuation of light in the tissue. However, in small animal geometries (~1-mm deep blood vessels), the SNR and experimental analysis (along with our prior experience) demonstrate that cells should be detectable. Because of the broad availability of GFP expressing cells, 488-nm DiFC is valuable in pre-clinical research. However, these data indicate that it is unlikely to be practical in translation to humans unless extremely bright fluorescent labeling can be achieved.

Second, for cases where cells are presumed to be present at larger depths (2 to 4 mm, as we expect in humans), SDS between 1 to 5 mm performed the best, with good general median coverage of the depth range observed for 3-mm separation. We plan to validate this experimentally in larger mammal models in the future. As expected, the highest detection SNR for a given depth was obtained using NIR wavelengths. Most of the recent class of fluorescence guided surgery molecular contrast agents for cancer are NIR,[14,41] some of which may ultimately be used as a contrast agent for DiFC. Likewise, circulating fluorescent sensors[7,42] can be engineered to emit light in NIR wavelengths.

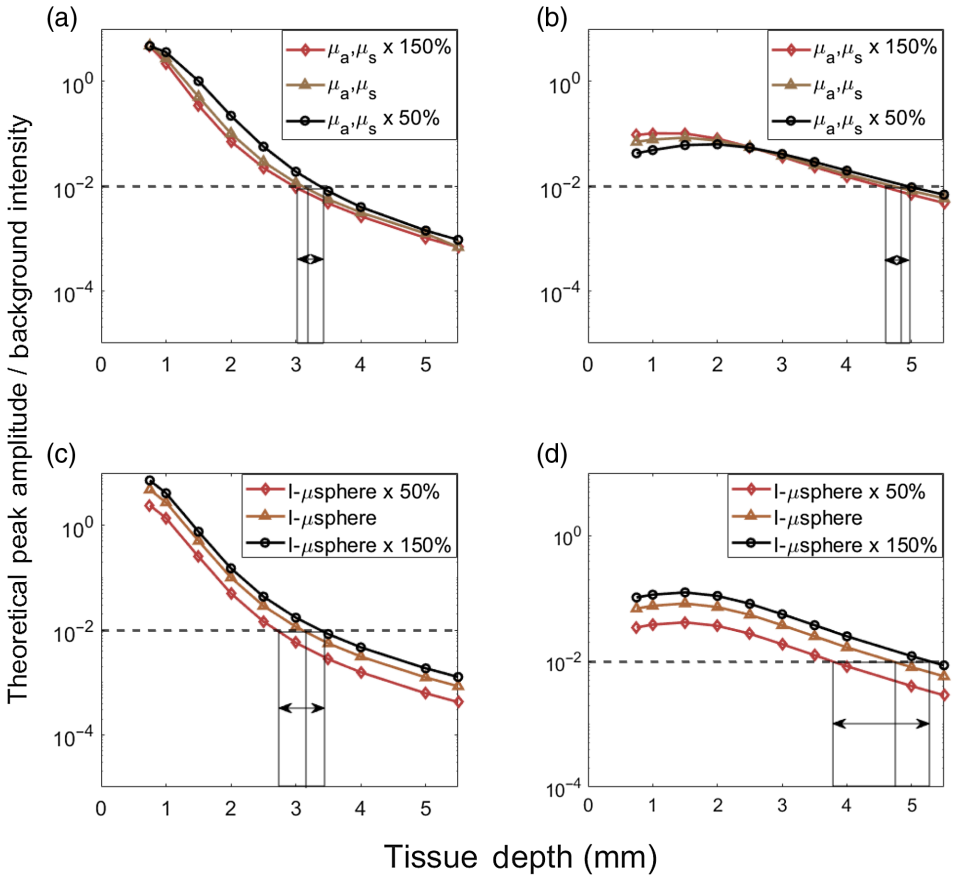

Fig. 7 (a) and (b) Estimated peak to background ratios for 780-nm light assuming 50% higher and 50% lower in optical properties for (a) 0.3-mm SDS and (b) 3 SDS, respectively. Estimated peak to background ratios assuming cell brightness 50% brighter 50% dimmer for (c) 0.3 mm, and (d) 3-mm SDS, respectively.

In summary, the most promising DiFC instrument geometry for potential human translation is with a SDS around 3 mm and using NIR fluorescent contrast agents. Experimental and computational analyses presented here suggest that this configuration should allow interrogation of human blood vessels located 2 to 4 mm under the skin, which is suitable for several major blood vessels that carry large circulating blood volumes. Evaluation and characterization of NIR contrast agents for CTCs is an ongoing area in our group.[15]

Disclosures

The authors have no conflicts of interests, financial or otherwise, to disclose.

Acknowledgments

This work was funded by the National Institutes of Health (Grant Nos. R21CA246413, R01-EB024186, and R01-GM114365).

Code, Data, and Materials Availability

MATLAB code and data for the Monte Carlo simulations, the laboratory experiments and the generation of the figures can be found in the GitHub open-source library, at https://github.com/mark-niedre/Ivich_depth_sensitivity_2022.

References

1. X. Tan et al., "*In vivo* flow cytometry of extremely rare circulating cells," *Sci. Rep.* **9**, 3366 (2019).
2. E. Zettergren et al., "Instrument for fluorescence sensing of circulating cells with diffuse light in mice *in vivo*," *J. Biomed. Opt.* **17**, 037001 (2012).
3. C. Hartmann et al., "Fluorescence detection, enumeration and characterization of single circulating cells *in vivo*: technology, applications and future prospects," *Phys. Med. Biol.* **63**, 01TR01 (2018).
4. R. Patil et al., "Fluorescence monitoring of rare circulating tumor cell and cluster dissemination in a multiple myeloma xenograft model *in vivo*," *J. Biomed. Opt.* **24**, 085004 (2019).
5. J. E. Fitzgerald et al., "Heterogeneity of circulating tumor cell dissemination and lung metastases in a subcutaneous Lewis lung carcinoma model," *Biomed. Opt. Express* **11**, 3633–3647 (2020).
6. A. L. Williams et al., "Short-term circulating tumor cell dynamics in mouse xenograft models and implications for liquid biopsy," *Front. Oncol.* **10**, 601085 (2020).
7. W. Di et al., "Real-time particle-by-particle detection of erythrocyte-camouflaged microsensor with extended circulation time in the bloodstream," *Proc. Natl. Acad. Sci. U. S. A.* **117**, 3509–3517 (2020).
8. M. Niedre, "Prospects for fluorescence molecular *in vivo* liquid biopsy of circulating tumor cells in humans," *Front. Photonics* **3**, 910035 (2022).
9. S. J. Cohen et al., "Relationship of circulating tumor cells to tumor response, progression-free survival, and overall survival in patients with metastatic colorectal cancer," *J. Clin. Oncol.* **26**, 3213–3221 (2008).
10. J. B. Smerage et al., "Circulating tumor cells and response to chemotherapy in metastatic breast cancer: SWOG S0500," *J. Clin. Oncol.* **32**, 3483–3489 (2014).
11. J. G. Moreno et al., "Circulating tumor cells predict survival in patients with metastatic prostate cancer," *Urology* **65**, 713–718 (2005).
12. X.-W. Cai et al., "Baseline plasma proteomic analysis to identify biomarkers that predict radiation-induced lung toxicity in patients receiving radiation for non-small cell lung cancer," *J. Thorac. Oncol.* **6**, 1073–1078 (2011).
13. J. Y. K. Lee et al., "Review of clinical trials in intraoperative molecular imaging during cancer surgery," *J. Biomed. Opt.* **24**, 120901 (2019).
14. S. Hernot et al., "Latest developments in molecular tracers for fluorescence image-guided cancer surgery," *Lancet Oncol.* **20**, e354–e367 (2019).
15. R. A. Patil et al., "Fluorescence labeling of circulating tumor cells with a folate receptor-targeted molecular probe for diffuse *in vivo* flow cytometry," *Mol. Imaging Biol.* **22**, 1280–1289 (2020).
16. V. Selvaraj and F. S. Buhari, "Ultrasound evaluation of effect of different degree of wrist extension on radial artery dimension at the wrist joint," *Ann. Card. Anaesth.* **19**, 63 (2016).
17. A. Masengu et al., "Preoperative radial artery volume flow is predictive of arteriovenous fistula outcomes," *J. Vasc. Surg.* **63**, 429–435 (2016).
18. S. Brigadoi and R. J. Cooper, "How short is short? Optimum source–detector distance for short-separation channels in functional near-infrared spectroscopy," *Neurophotonics* **2**, 025005 (2015).
19. N. Sujatha, K. B. Nivetha, and A. Singhal, "Optimal source to detector separation for extracting sub-dermal chromophores in fiber optic diffuse reflectance spectroscopy: a simulation study," *Proc. SPIE* **9129**, 91291P (2014).
20. G. Han et al., "Optimization of source-detector separation for non-invasive regional cerebral blood flow sensing," *Infrared Phys. Technol.* **117**, 103843 (2021).
21. K.-B. Sung and H.-H. Chen, "Enhancing the sensitivity to scattering coefficient of the epithelium in a two-layered tissue model by oblique optical fibers: Monte Carlo study," *J. Biomed. Opt.* **17**, 107003 (2012).
22. G. E. Strangman, Z. Li, and Q. Zhang, "Depth sensitivity and source-detector separations for near infrared spectroscopy based on the Colin27 brain template," *PLoS ONE* **8**, e66319 (2013).

23. L. Wang, H. Ayaz, and M. Izzetoglu, "Investigation of the source-detector separation in near infrared spectroscopy for healthy and clinical applications," *J. Biophotonics* **12** (2019).
24. C. Ash et al., "Effect of wavelength and beam width on penetration in light-tissue interaction using computational methods," *Lasers Med. Sci.* **32**, 1909–1918 (2017).
25. Q. Liu, C. Zhu, and N. Ramanujam, "Experimental validation of Monte Carlo modeling of fluorescence in tissues in the UV-visible spectrum," *J. Biomed. Opt.* **8**, 223 (2003).
26. J. Pace et al., "Near infrared diffuse *in vivo* flow cytometry," biorxiv, 2022.05.11.491330 (2022).
27. Q. Fang and D. A. Boas, "Monte Carlo simulation of photon migration in 3D turbid media accelerated by graphics processing units," *Opt. Express* **17**, 20178 (2009).
28. L. Yu et al., "Scalable and massively parallel Monte Carlo photon transport simulations for heterogeneous computing platforms," *J. Biomed. Opt.* **23**, 010504 (2018).
29. S. L. Jacques, "Optical properties of biological tissues: a review," *Phys. Med. Biol.* **58**, R37–R61 (2013).
30. S. Brooks et al., "Sources of variability in the quantification of tissue optical properties by multidiameter single-fiber reflectance and fluorescence spectroscopy," *J. Biomed. Opt.* **20**, 057002 (2015).
31. R. Yao, X. Intes, and Q. Fang, "Direct approach to compute Jacobians for diffuse optical tomography using perturbation Monte Carlo-based photon 'replay'," *Biomed. Opt. Express* **9**, 4588 (2018).
32. E. Zettergren et al., "Tomographic sensing and localization of fluorescently labeled circulating cells in mice *in vivo*," *Phys. Med. Biol.* **57**, 4627–4641 (2012).
33. B. Ten et al., "Evaluation of facial artery course variations and depth by Doppler ultrasonography," *J. Cosmet. Dermatol.* **20**, 2247–2258 (2021).
34. E. I. Galanzha and V. P. Zharov, "Photoacoustic flow cytometry," *Methods* **57**, 280–296 (2012).
35. D. A. Nedosekin et al., "*In vivo* noninvasive analysis of graphene nanomaterial pharmacokinetics using photoacoustic flow cytometry," *J. Appl. Toxicol.* **37**, 1297–1304 (2017).
36. G. S. L. Teo et al., "Intravital imaging of mesenchymal stem cell trafficking and association with platelets and neutrophils," *Stem Cells* **33**, 265–277 (2015).
37. J. W. Wu et al., "Intravital fluorescence microscopy with negative contrast," *PLoS One* **16**, e0255204 (2021).
38. K. Pang et al., "Recent advances in fluorescence-based *in vivo* flow cytometry," *J. Innov. Opt. Health Sci.* **12**, 1930008 (2019).
39. A. K. Gaigalas et al., "Quantitating fluorescence intensity from fluorophore: assignment of MESF values," *J. Res. Natl. Inst. Stand. Technol.* **110**, 101–114 (2005).
40. S. Ismail, U. Akram, and I. Siddiqi, "Heart rate tracking in photoplethysmography signals affected by motion artifacts: a review," *EURASIP J. Adv. Signal Process.* **2021**, 5 (2021).
41. Y. Zhang et al., "Design and application of receptor-targeted fluorescent probes based on small molecular fluorescent dyes," *Bioconjug. Chem.* **32**, 4–24 (2021).
42. J. Morales et al., "DNA-based photoacoustic nanosensor for interferon gamma detection," *ACS Sens.* **4**, 1313–1322 (2019).

Fernando Ivich received his BS and MS degrees in biomedical engineering from the University of Arizona in 2017 and 2019, respectively. He is a PhD candidate in the Northeastern University Department of Bioengineering.

Joshua Pace received his BS degree in biomedical engineering from the University of Arizona in 2019. He is currently a PhD candidate in the Northeastern University Department of Bioengineering.

Mark Niedre received his PhD from the University of Toronto in medical physics in 2004. He is a professor of bioengineering at Northeastern University and a senior member of SPIE.

Biographies of the other authors are not available.